forum acusticum 2026
8-12 September · Graz, Austria

Dynamic acoustic field modeling of internal solitary waves in the South China Sea and their impact on hydroacoustic detection

Lintai Rong[1,2], Bo Lei[1,2]

[1] *School of Marine Science and Technology, Northwestern Polytechnical University, China*
[2] *Shaanxi Key Laboratory of Underwater Information Technology, Northwestern Polytechnical University, Xi'an, China*

This paper is a revised version of the authors' submitted manuscript that was peer-reviewed by at least two anonymous reviewers.

Abstract

The South China Sea (SCS) is one of the most active regions for the internal solitary wave (ISW). During the ISW propagation, strong sound-speed perturbations can be induced, leading to anomalous underwater acoustic propagation phenomena, which have a significant impact on hydroacoustic detection. To quantitatively asses these impacts, this study considers three representative ISW on the northern SCS continental slope. Time-varying acoustic field models are constructed, and numerical simulations are conducted to evaluate the source localization errors and the horizontal deflection of acoustic propagation in ISW-affected environments. The results indicate that, across the three ISW cases, the mean localization error rates in source range and depth reach 10% and 15%, respectively, while the maximum horizontal deflection angle reaches 8°. Furthermore, when the ISWs passes through the source, the mode-1 single ISW causes acoustic waves propagating along the wave-crest direction to be deflected outward, away from the crest. In contrast, the mode-2 single ISW produces the weakest horizontal deflection for its smaller amplitude and the presence of a near-surface low-sound-speed layer. For the mode-1 ISW packet, multiple constituent waves induce repeated bending of acoustic propagation paths, resulting in a more persistent influence over time.

Keywords: *Internal solitary wave, Acoustic field modeling, Underwater acoustic detection, Horizontal deflection*

1. Introduction

Internal solitary waves (ISWs) are a common submesoscale oceanic phenomenon in the northern South China Sea (SCS). They are primarily generated by tide-topography interactions in the Luzon Strait and subsequently evolve during westward propagation [1]. The ISW with strong nonlinearity can induce pronounced local perturbations in seawater temperature, density, and sound speed during its propagation, thereby changing the underwater acoustic field over multiple spatial and temporal scales and exerting a substantial impact on hydroacoustic detection [2], [3].

In recent years, researchers have primarily focused on characterizing how ISW affect the underwater acoustic fields. With respect to the sound-speed field modeling of the ISW, many studies approximate the water column as two layers separated by a pycnocline (i.e., a two-layer ocean model) with distinct density and sound speed [4]. This assumption simplifies the numerical implementation, while it can lead to non-negligible biases when the seawater stratification is weak or the pycnocline is not sharply defined [5]. In some studies, the sound-speed field of the ISW is constructed directly from in-situ observations. Although such analyses provide high authenticity, they are often limited to case-specific scenarios [6]. Meanwhile, high-resolution ocean numerical models (such as MIT General Circulation Model and Finite Volume Community Ocean Model, etc) have also been employed to simulate the generation, propagation, and evolution of the ISWs in a fully three-dimensional framework, but their broader application remains constrained by substantial computational cost [3], [7].

In addition, most existing hydroacoustic studies focus on acoustic field characteristics associated with the mode-1 ISW (packet). However, oceanographic observations indicate that the mode-2 ISWs are also prevalent in the northern SCS during winter [8], [9]. The mode-2 ISWs exhibit a distinct vertical structure (typically characterized by an upper-layer elevation and a lower-layer depression) and induce acoustic propagation effects that differ markedly from those produced by the mode-1 ISWs.

Corresponding author: *lei.bo@nwpu.edu.cn.*

Against the above background, this study considers three representative types of the ISWs (mode-1 single ISW, mode-2 single ISW, and mode-1 ISW packet) commonly observed over the continental slope near the Dongsha Island in the northern SCS. The time-varying sound-speed fields during the ISW propagation are modeled numerically, and the corresponding three-dimensional acoustic fields are simulated based on ray acoustic model. Building on theses simulations, we quantitatively analyze and compare the source localization errors (via matched-field processing) and the horizontal deflection of acoustic propagation under the ISW conditions, providing a useful reference for assessing hydroacoustic detection performance in the ISW-affected environments.

2. Theory and Methods

2.1 Modeling of the ISW-induced sound-speed field

The Korteweg-de Vries (KdV) equation [10], as a one-dimensional governing equation derived under the assumptions of shallow water and small amplitude, has been widely used to describe the ISW disturbances occurring near the oceanic pycnocline. However, in continental-slope regions where the ISWs are concentrated, rapid bathymetric variations lead to pronounced spatial variability in properties of the ISW. Therefore, it is necessary to take into account factors such as the horizontal inhomogeneity in both water-column stratification and bathymetry. Correspondingly, the classical KdV equation is modified as follows [11]:

$$\frac{\partial \eta}{\partial t} + (v_0 + \alpha\eta)\frac{\partial \eta}{\partial x} + \beta\frac{\partial^3 \eta}{\partial x^3} + \frac{v_0}{2Q}\frac{dQ}{dx}\eta = 0, \qquad (1)$$

where $\eta(x,t)$ is the displacement of the pycnocline. α, β, and Q denote the nonlinear coefficient, the dispersive coefficient, and the correction coefficient associated with external forcing (e.g., variations in bathymetry or the oceanic medium), respectively. Their expressions are given as follows:

$$\alpha = \frac{3\int_{-H}^{0}(v-U)^2(d\phi/dz)^3\,dz}{2\int_{-H}^{0}(v-U)(d\phi/dz)^2\,dz}, \qquad (2)$$

$$\beta = \frac{\int_{-H}^{0}(v-U)^2\phi^2\,dz}{2\int_{-H}^{0}(v-U)(d\phi/dz)^2\,dz}, \qquad (3)$$

$$Q = \frac{v^2\int_{-H}^{0}(v-U)(d\phi/dz)^2\,dz}{v_0^2\int_{-H}^{0}(v_0-U_0)(d\phi_0/dz)^2\,dz}, \qquad (4)$$

where H and z denote the seawater depth and the vertical coordinate (positive upward), respectively. v_0 and U_0 represent the linear phase speed of the ISW and the horizontal velocity of the background current in the initial state, respectively. v and U denote the linear phase speed and background current at subsequent times (or at different ranges) during the ISW propagation. ϕ_0 and ϕ are the vertical modal functions of the ISW for the initial state and for the subsequent propagation stage, respectively.

The propagation process of the ISW can be regarded as a sequence of discrete "time snapshots", and the solution of Eq. (1) at a given time (snapshot) is referred to as the stationary solution. For a single ISW, the solution can be expressed as:

$$\eta(x,t) = \frac{\eta_0}{\sqrt{Q}}sech^2\left(\frac{x+v't}{\sqrt{12\beta/(\alpha\eta_0)}}\right), \qquad (5)$$

where η_0 denotes the initial amplitude of the ISW, and $v' = v + \alpha\eta/3$ is the nonlinear phase speed (i.e., the propagation speed) of the ISW.

For an ISW packet, the solution (given by the cnoidal-wave solution of the KdV equation) can be expressed as follows:

$$\eta(x,t) = \eta_0\left\{dn_s^2\left[\frac{\sqrt{\alpha\eta/(3\beta)}(x+v't)}{2}\right] - \frac{1+s^2}{2}\right\}, \qquad (6)$$

$$v' = v\left(1 + \frac{1+s^2}{6}\alpha\eta\right), \qquad (7)$$

where η_0 denotes the initial amplitude of the leading wave in the wave packet. dn_s represents a Jacobi elliptic function with modulus s. s^2 is a nonlinearity parameter, which is determined by:

$$-2\frac{x+vt}{\alpha\eta t} = \frac{1+s^2}{3} - \frac{2}{3}\frac{s^2(1-s^2)K(s)}{E(s)-(1-s^2)K(s)}, \qquad (8)$$

where $K(s)$ and $E(s)$ denote the complete elliptic integrals of the first and second kinds, respectively.

Under continuously stratified ocean conditions, the linear phase speed v (v_0) and the corresponding vertical modal function ϕ (ϕ_0) can be obtained by solving the following Taylor-Goldstein equation [12]:

$$\frac{d}{dz}\left[(v-U)^2\frac{d\phi}{dz}\right] + N^2\phi = 0, \qquad (9)$$

$$\phi(-H) = 0, \qquad (10)$$

$$(v-U)^2\frac{d\phi(0)}{dz} = g\phi(0), \qquad (11)$$

where $N(z)$ and g denote the buoyancy frequency and gravitational acceleration, respectively. Equations (10) and (11) correspond to the rigid-lid bottom boundary and the free-surface boundary condition, respectively.

Furthermore, for the single ISW, by substituting the v (v_0) and ϕ (ϕ_0) obtained from Eq. (9) into Eq. (5), the vertical displacement field of the ISW over the entire water column can be expressed as:

$$\eta(x,z,t) = \frac{\eta_0}{\sqrt{Q}}\phi^{(j)}sech^2\left[\frac{x+v'^{(j)}t}{\sqrt{12\beta/(\alpha\eta_0)}}\right], \qquad (12)$$

where $j = 1,2$ represents the mode-1 and mode-2 ISW, respectively.

Similarly, substituting the $v'^{(1)}$ and $\phi^{(1)}$ of the mode-1 ISW into Eq. (6), the vertical displacement field of the ISW packet over the entire water column can be expressed as:

$$\eta(x,z,t) = \frac{\eta_0 \phi^{(1)}}{\sqrt{Q}} \cdot \left\{ dn_s^2 \left[\sqrt{\frac{4\alpha\eta}{3\beta}} \left(x + v'^{(1)} t\right) \right] - \frac{1+s^2}{2} \right\}. \quad (13)$$

Based on the above theory, the time-varying sound-speed field of the ISW (C_{ISW}) can be constructed from the background sound-speed field (C_{BG}) at the initial time (without the ISW) and the $\eta(x,z,t)$, as follows:

$$C_{ISW}(x,z,t) = C_{BG}(x,z_i) + \frac{[C_{BG}(x,z_{i+1}) - C_{BG}(x,z_i)][z - z_i + \eta(x,z_i,t)]}{[z_{i+1} - \eta(x,z_{i+1},t)] - [z_i - \eta(x,z_i,t)]}, \quad (14)$$

where $i = 1, \cdots, M$ indexes the number of stratified layers in the seawater column.

2.2 Matched-field processing localization

Matched-field processing (MFP) is a model-based signal processing technique in which an acoustic propagation model is used to compute replica fields that are matched to measured array data to estimate the source location. The Bartlett processor is a prototypical linear MFP processor and is relatively insensitive to environmental mismatch and amplitude/phase errors of array, thereby offering strong robustness and remaining one of the most widely used processors in practical applications [13], [14]. The broadband incoherent Bartlett MFP can be expressed as follows:

$$P(r,z) = \frac{1}{M_f} \sum_{j=1}^{M_f} a^H(r,z,f_j) K(f_j) a(r,z,f_j), \quad (15)$$

where r, z, and f_j denote the range, depth, and frequency of the source, respectively. M_f represent the number of the processing frequency points. a is the normalized replica vectors. H denotes the Hermitian operator. The sample covariance matrix K at frequency f_j is obtained using L snapshots:

$$K(f_j) = \frac{1}{L} \sum_{l=1}^{L} y_l(f_j) y_l^H(f_j), \quad (16)$$

where represents the complex signal spectrum received by the array of the lth data segment at frequency f_j. The r and z corresponding to the maximum Bartlett power P are the estimated location of the source.

3. Simulation and Analysis

3.1 Simulation environment

The simulation environment is illustrated in Fig. 1. A transect of ~20 km located to the northeast of Dongsha Island in the SCS, aligned with predominant northwestward propagation direction of the ISWs [8], is selected as the study bathymetry (green line in Fig. 1b). Along this transect, the seawater depth varies from 260 m to 630 m, representative of a typical continental slope (Fig. 1a). In addition, the background sound-speed profile (SSP) in this region exhibits an overall negative vertical gradient. The near-surface mixed-layer thickness is ~10 m in summer (orange curve in Fig. 1a) and increased to ~60 m in winter (blue curve in Fig. 1a). Since the mode-1 and mode-2 ISWs are more active in summer and winter, respectively, the construction of the sound-speed fields for the mode-1 and mode-2 ISWs in the subsequent simulations is based on the summer and winter SSP accordingly. The bathymetric and SSP data used in this study are obtained from the GEBCO [15] and HYCOM datasets [16], respectively. The acoustic field is simulated utilizing the Bellhop3D ray-based model [17].

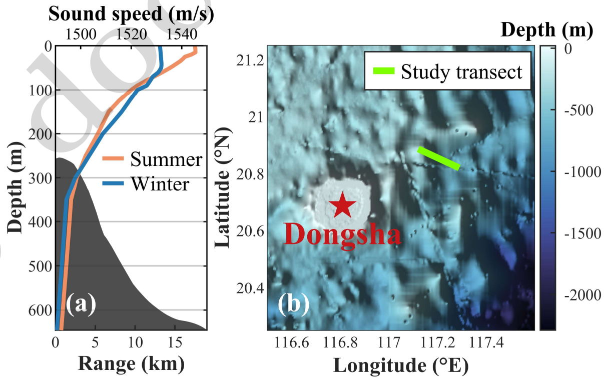

Figure 1. (a) Bathymetric profile along the simulation transect and the summer and winter background SSP. (b) Seafloor bathymetry over the northern SCS continental slope and the study transect (green line).

Based on observation results in the study region, the mode-1 single ISWs exhibit relatively large amplitudes, with peak values reaching on the order of 100 m [18]. In contrast, the mode-2 single ISWs are characterized by upper-layer elevation and lower-layer depression, and generally have smaller amplitudes with broader wave width. For the mode-1 ISW packets, the leading wave has the largest amplitude and the narrowest width, whereas the trailing waves progressively decrease in amplitude and broaden in waveform. Accordingly, the initial maximum amplitudes are set to 80 m for the mode-1 single ISW, 60 m for the mode-2 single ISW, and 80 m for the mode-1 ISW packet in this study. Fig. 2 shows the temporal evolution of the isovelocity contours (i.e., the waveforms) at a depth of 150 m during the climbing process of the above three types of the ISWs. Owing to bathymetric effects, energy is dissipated as the ISWs propagate upslope, leading to a gradual reduction in amplitude and a progressive broadening of the waveforms. In addition, the mode-2 single ISW undergoes a polarity reversal, transitioning from a depression-type to an elevation-type structure (Fig. 2b).

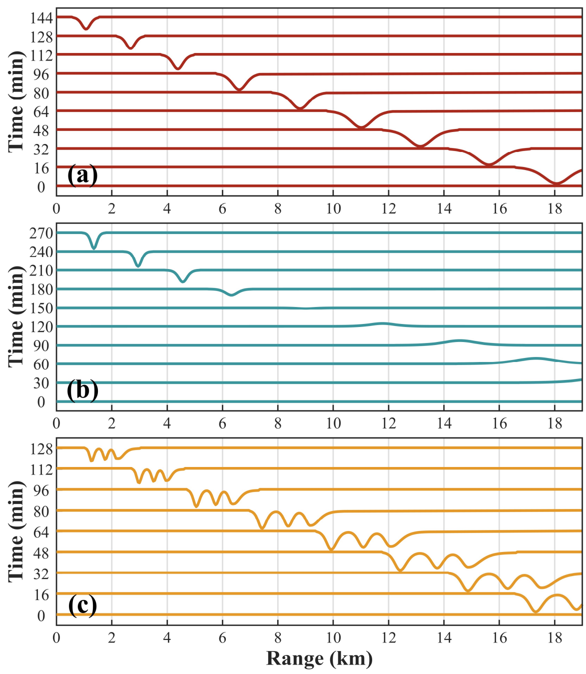

Figure 2. Temporal evolution of the isovelocity contours at a depth of 150 m during the climbing process of the (a) mode-1 single ISW, (b) mode-2 single ISW, and (c) mode-1 ISW packet.

3.2 MFP localization error analysis

To quantify the impact of the ISWs on source localization, an upslope broadband source (50-250 Hz) and a bottom-moored vertical line array on the downslope (with 32 element and spacing of 5 m) are considered in this section, where the source depth is 100 m, and the horizontal range from the source to the array is 8 km. Fig. 3 presents the broadband Bartlett power (ambiguity surface) in the absence of the ISW. As shown, when no ISW is present, the accurate estimation of the source location can be achieved since there is no sound-speed field mismatch.

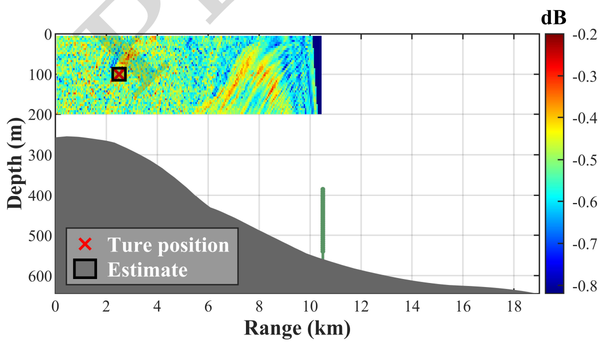

Figure 3. Schematic of the source location (red cross) and the vertical line array (green dotted line), together with the MFP ambiguity surface (colormap in the upper-left panel) in the absence of the ISW.

Furthermore, the MFP localization errors during the ISWs propagation are analyzed. The localization error rate η is defined as follows:

$$\eta = \frac{|\tilde{\theta} - \theta_S|}{\theta_S} \times 100\%, \tag{17}$$

where θ_S and $\tilde{\theta}$ denote the true source location and the estimation, respectively.

As shown in Fig. 4, although the ISWs cause fluctuation in the signal-to-noise (SNR) at the array by ~5 dB during the propagation, the SNR variations are not the primary driver of the increased MFP localization errors. Instead, the dominant factor is the sound-speed field mismatch due to the ISW. Under the influence of the three ISW scenarios, the mean estimation error rates in source range and depth reach ~10% and ~15%, respectively. Notably, although the mode-2 ISW has smallest amplitude, it exhibits the largest wave width (and thus the broadest area of influence), resulting in the largest localization errors.

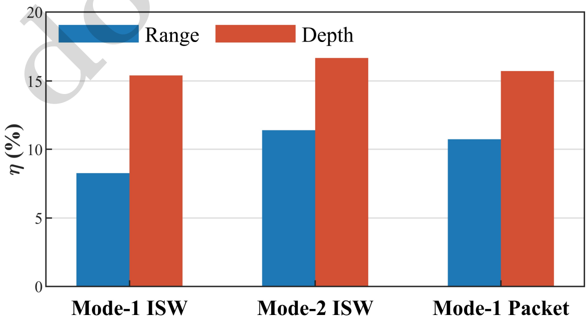

Figure 4. Mean estimation error rates in source range (blue bars) and depth (red bars) during the propagation of the three ISW types.

3.3 Horizontal deflection effects on acoustic propagation

ISWs not only induce pronounced oscillations in the vertical acoustic field but, owing to their extended crest lengths (typically on the order of hundreds of kilometers), can also cause horizontal deflection of acoustic propagation, thereby affecting the direction-of-arrival (DOA) estimation. In this section, the horizontal deflection induced by the ISWs during their passage across the source region (when the horizontal deflection is most pronounced) was evaluated quantitatively, and the analysis was carried out from the perspective of ray acoustics.

Fig. 5-Fig. 7 depict the horizontal deflection of acoustic rays launched at azimuths of 30°, 60°, and 90° (Y-axis) during the passage of the three ISW types across the source region, where the location of the source is (X=2.5 km, Y=0 km). The semi-transparent magenta rectangle indicates the ISW-influenced zone, and the

magenta solid lines denotes the crests of the ISW (or its constituent sub-waves). The left side (shallower region) and right side (deeper region) of each crest correspond to the pre-crest and post-crest status, respectively. In addition, the bathymetry is assumed invariant along the Y-axis, while along the X-axis it follows the profile shown in Fig. 1a. The propagation direction of the ISW is orthogonal to the contour lines of the terrain.
The mode-1 single ISW (with a depression waveform) transports high-sound-speed seawater in the upper ocean downward, such that, at a given depth, the ISW-influenced region is characterized by higher sound-speed than the adjacent seawaters on both sides, where the sound-speed is lower. Consequently, before and after the crest of the mode-1 single ISW passes the source, acoustic rays launched along the crest direction (Y-axis) are deflected toward the pre-crest and post-crest sides, respectively (green solid curves in Fig. 5). In contrast, rays launched opposite to the ISW propagation direction (X-axis) exhibits negligible horizontal deflection, whereas rays launched at azimuths of 30° (yellow lines) and 60° (red lines) are deflected toward deeper water due to the continental-slope bathymetry.

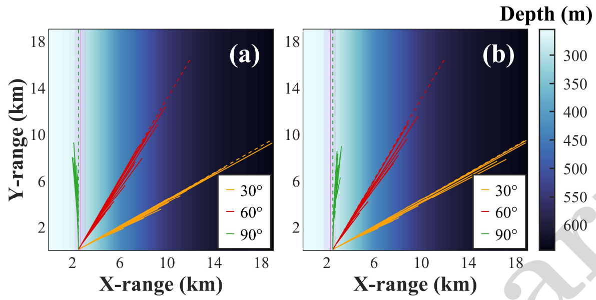

Figure 5. Horizontal deflection of acoustic rays launched in different horizontal azimuths (dashed lines) when the source is located (a) ahead of and (b) behind the crest of the mode-1 single ISW. The corresponding deflected ray paths are shown by solid lines.

Unlike the mode-1 single ISW, the mode-2 single ISW exhibits an elevation structure in the upper layer and transports low-sound-speed seawater from the lower layer upward. As a result, acoustic rays launched along the crest direction tend to focus toward the ISW-influenced region with lower sound-speed. However, when the mode-2 ISW propagates into the upslope area, the depression component near the source depth becomes dominant (Fig. 2b). Consequently, most launched rays are still deflected toward both sides of the mode-2 single ISW (similar to the mode-1 single ISW) with only a small fraction of rays focusing within the ISW-influenced region (Fig. 6).

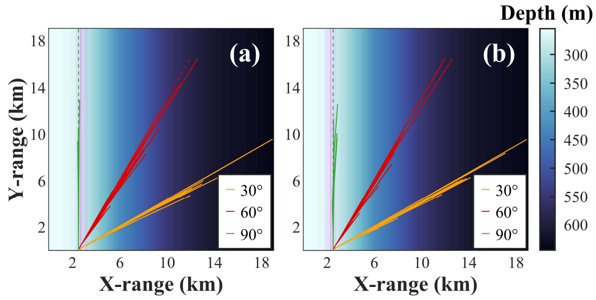

Figure 6. Horizontal deflection of acoustic rays launched in different horizontal azimuths (dashed lines) when the source is located (a) ahead of and (b) behind the crest of the mode-2 single ISW. The corresponding deflected ray paths are shown by solid lines.

When the mode-1 ISW packet passes the source region, the horizontal deflection behavior of the acoustic rays is broadly similar to that observed for the mode-1 single ISW, because the packet consists of multiple mode-1 constituent waves. However, since the pre-crest and post-crest regions of adjacent sub-waves are contiguous, rays undergo multiple successive horizontal deflections within the ISW-influenced zone rather than being steered predominantly toward a single direction. The ray bending curvature is also markedly enhanced, yielding a maximum horizontal deflection angle of up to 8°.

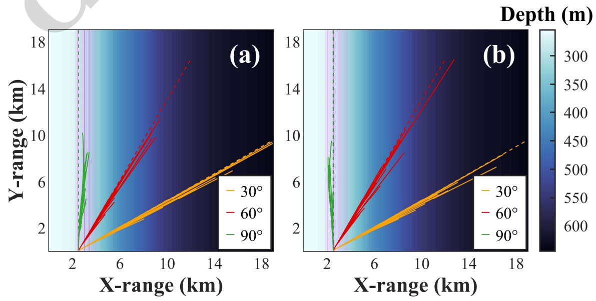

Figure 7. Horizontal deflection of acoustic rays launched in different horizontal azimuths (dashed lines) when the source is located (a) ahead of and (b) behind the crest of the mode-1 ISW packet. The corresponding deflected ray paths are shown by solid lines.

4. Conclusion

This study presents a time-varying, continuously stratified modeling framework for the ISW-induced sound-speed fields. Utilizing the ray-based acoustic model, the 3D acoustic simulations for three representative ISW (mode-1 single ISW, mode-2 single ISW, and mode-1 ISW packet) scenarios over the Dongsha continental slope in the SCS were performed. On this basis, the impacts of the ISWs on MFP localization performance as well as the ISW-induced horizontal deflection are evaluated quantitatively.
The results demonstrated that the mismatch of the ISW-induced sound-speed field is the primary factor for the decline in performance of the MFP, where the mean estimation error rates in source range and depth reach

10% and 15%, respectively. Although the amplitude of the mode-2 single ISW is relatively small, due to its broader wave width and the polarity reversal, the resulting MFP localization error is the largest.
In addition, the ISWs produce pronounced horizontal deflection that can affect the DOA estimation. The mode-1 single ISW deflects crest-directed acoustic rays toward the pre-crest or post-crest side depending on the source position relative to the crest, while the mode-1 ISW packet induced multiple successive deflections within the ISW-influenced region, leading to enhanced ray curvature with the maximum horizontal deflection angle of 8°. This study elucidates the anomalous acoustic propagation phenomena from the perspective ray acoustics, and provides a useful reference for assessing hydroacoustic detection performance in the ISW environments.

References

[1] C. Guo and X. Chen: "A review of internal solitary wave dynamics in the northern South China Sea," *Progress in Oceanography*, vol. 121, pp. 7–23, 2014.

[2] F. Gao, P. Hu, F. Xu, Z. Li, and J. Qin: "Effects of internal waves on acoustic temporal coherence in the South China Sea," *Journal of Marine Science and Engineering*, vol. 11, no. 2, p. 374, 2023.

[3] J. Li, X. Huang, Y. Shi, and W. Zhao: "Effects of internal solitary waves on three-dimensional sound propagation and DOA estimation in the South China Sea," *Applied Acoustics*, vol. 212, p. 109612, 2023.

[4] Y. Feng, Q. Tang, J. Li, J. Sun, and W. Zhan: "Internal solitary waves observed on the continental shelf in the northern south China Sea from acoustic backscatter data," *Frontiers in Marine Science*, vol. 8, p. 734075, 2021.

[5] C. Xu, Z. Wang, and H. Masoud: "Error calculation of large-amplitude internal solitary waves within the pycnocline introduced by strong stratification approximation," *Journal of Marine Science and Application*, vol. 22, no. 1, pp. 146–152, 2023.

[6] T. Chen, Y. Lin, L. Chiu, and W. Siegmann: "Observation and modeling of three-dimensional sound propagation along a nonlinear internal gravity wave at a shelfbreak," *The Journal of the Acoustical Society of America*, vol. 157, no. 2, pp. 857–865, 2025.

[7] Z. Lai, G. Jin, Y. Huang, H. Chen, X. Shang, and X. Xiong: "The generation of nonlinear internal waves in the South China Sea: A three – dimensional, nonhydrostatic numerical study," *Journal of Geophysical Research: Oceans*, vol. 124, no. 12, pp. 8949–8968, 2019.

[8] L. Chen, Q. Zheng, X. Xiong, Y. Yuan, H. Xie, Y. Guo, L. Yu, and S. Yun: "Dynamic and statistical features of internal solitary waves on the continental slope in the northern South China Sea derived from mooring observations," *Journal of Geophysical Research: Oceans*, vol. 124, no. 6, pp. 4078–4097, 2019.

[9] L. Rong, X. Xiong, and L. Chen: "Assessment of KdV and EKdV theories for simulating internal solitary waves in the continental slope of the South China Sea," *Continental Shelf Research*, vol. 256, p. 104944, 2023.

[10] D. Kortweg and V. De: "On the change of form of long waves advancing in a rectangular canal, and on a new type of long stationary waves," *Philosophical Magazine*, vol. 91, no. 4–6, pp. 1007–1028, 2011.

[11] P. Holloway, E. Pelinovsky, T. Talipova, and B. Barnes: "A nonlinear model of internal tide transformation on the Australian North West Shelf," *Journal of Physical Oceanography*, vol. 27, no. 6, pp. 871–896, 1997.

[12] R. Grimshaw, E. Pelinovsky, T. Talipova, and O. Kurkina: "Internal solitary waves: propagation, deformation and disintegration," *Nonlinear Processes in Geophysics*, vol. 17, no. 6, pp. 633–649, 2010.

[13] A. Baggeroer, W. Kuperman, and P. Mikhalevsky: "An overview of matched field methods in ocean acoustics," *IEEE Journal of Oceanic Engineering*, vol. 18, no. 4, pp. 401–424, 2002.

[14] R. Zhang, Z. Li, J. Yan, Z. Peng, and F. Li: "Broad-band matched-field source localization in the East China Sea," *IEEE Journal of Oceanic Engineering*, vol. 29, no. 4, pp. 1049–1054, 2004.

[15] B. Tozer, D. Sandwell, W. Smith, C. Olson, J. Beale, and P. Wessel: "Global bathymetry and topography at 15 arc sec: SRTM15+," *Earth and space science*, vol. 6, no. 10, pp. 1847–1864, 2019.

[16] E. Chassignet, H. Hurlburt, O. Smedstad, G. Halliwell, P. Hogan, A. Wallcraft, R. Baraille, and R. Bleck: "The HYCOM (hybrid coordinate ocean model) data assimilative system," *Journal of Marine Systems*, vol. 65, no. 1–4, pp. 60–83, 2007.

[17] M. Porter: "Beam tracing for two- and three-dimensional problems in ocean acoustics," *The Journal of the Acoustical Society of America*, vol. 146, no. 3, pp. 2016–2029, 2019.

[18] X. Huang, Z. Chen, W. Zhao, Z. Zhang, C. Zhou, Q. Yang, and J. Tian: "An extreme internal solitary wave event observed in the northern South China Sea," *Scientific reports*, vol. 6, no. 1, pp. 30041, 2016.